

Image to Images Translation for Multi-Task Organ Segmentation and Bone Suppression in Chest X-Ray Radiography

Mohammad Eslami, Solale Tabarestani, Shadi Albarqouni, Ehsan Adeli, Nassir Navab, and Malek Adjouadi,

Abstract—Chest X-ray radiography is one of the earliest medical imaging technologies and remains one of the most widely used for the diagnosis, screening and treatment follow up of diseases related to lungs and heart. The literature in this field of research reports many interesting studies dealing with the challenging tasks of bone suppression and organ segmentation but performed separately, limiting any learning that comes with the consolidation of parameters that could optimize both processes. Although image processing could facilitate computer aided diagnosis, machine learning seems more amenable in dealing with the many parameters one would have to contend with to yield an near optimal classification or decision-making process. This study, and for the first time, introduces a multitask deep learning model that generates simultaneously the bone-suppressed image and the organ segmented image, minimizing as a consequence the number of parameters the model has to deal with and optimizing the processing time as well; while at the same time exploiting the interplay in these parameters so as to benefit the performance of both tasks. The design architecture of this model, which relies on a conditional generative adversarial network, reveals the process on how we managed to modify the well-established pix2pix network to fit the need for multitasking and hence extending the standard image-to-image network to the new image-to-images architecture. Dilated convolutions are also used to improve the results through a more effective receptive field assessment. A comparison of the proposed approach to state-of-the-art algorithms is provided to gauge the merits of the proposed approach.

Index Terms—chest X-Ray, CXR imaging, organ segmentation, bone suppression, multi-task deep learning, image-to-image translation, image-to-images translation.

I. INTRODUCTION

Chest radiography, also called chest X-ray or CXR, is one of the most affordable and widely used medical imaging modalities which has significant practical implications in the diagnosis and screening of the thorax region and the organs and bone structure within it. Over 2 billion procedures per year are performed using this technology for the purpose of medical diagnosis of a variety of diseases, such as pneumonia, tuberculosis, lung cancer and heart failure. Moreover, chest

M. Eslami is with RWTH Aachen University, RWTH University Hospital, Aachen, Germany, email: meslami@ukaachen.de. This work is done while Eslami was a visiting scholar at CAMP.

S. Albarqouni and N. Navab are with Computer Aided Medical Procedures and Augmented Reality (CAMP), Technical University of Munich (TUM), Munich, Germany.

S. Tabarestani and M. Adjouadi are with Center for Advanced Technology and Education (CATE), Florida International University, Miami, USA.

E. Adeli is with Stanford University, Stanford, CA, USA.

radiography remains the most prevalent screening test for pulmonary disorders [54]–[56]. Due to overlapping organs, low resolution and subtle anatomical shape and size variations, interpreting CXR images accurately remains challenging and requires well-trained staff. On the other hand, managing a large number of CXR images each day results in high workloads for the radiography staff, yielding a tedious process fraught with setbacks and errors in diagnosis and in assessing adequately treatment follow up. It is reported that almost 90 percent of mistakes in pulmonary tumor diagnosis could be associated with the CXR screening of images [32]. Therefore, many efforts have been devoted to the development of automated computer-based methods to improve accuracy in diagnosis and finding abnormalities [2], [3], [48].

Among the more recent work on chest radiography, Rajpurkar et al. [30] proposed a convolutional neural network called CheXNeXt as a deep learning algorithm to concurrently detect the presence of 14 different pathologies such as pneumonia, fibrosis, emphysema and nodules in frontal-view chest radiographs, among others. The CheXNeXt algorithm achieved promising results in identifying abnormalities at a performance level that was comparable with the diagnostic accuracy of radiologist practitioners. This CheXNeXt algorithm was introduced earlier as a 121-layer convolutional neural network in [31]. Diamant et al. [48] employed ResNet network appended with transfer learning to categorize the pathology in CXR images. In another research endeavor [33], the authors proposed the deep multi-Instance learning (DMIL) algorithm, which combines in an interesting way deep learning and multi-instance learning to detect abnormal images, enlarged heart and pulmonary nodule(s). In another study, [32] Gozes and Greespan proposed a method to improve the contrast of lung structures in CXR images leading to better accuracy in nodule(s) detection; while Wang and Chia proposed a deep neural network they named ChestNet [50] for enhanced diagnosis of diseases on chest radiography.

In this work, we introduce a multitask learning framework using deep learning techniques that address in an effective way the two challenging tasks of organ segmentation and bone suppression simultaneously. Organ segmentation is used for computer-aided detection and diagnosis while bone suppression enhances the visibility of the disease effects e.g. nodules particularly on the lung region.

A. Task 1: Organ Segmentation

Organ segmentation is one of the most difficult tasks in medical imaging due in large part to the elusive thresholding process and the ubiquitous presence of noise [57], [58], but is an essential for delineating the anatomical structures of organs and hence for detecting abnormalities such as enlarged heart or collapsed lungs. It should be noted that when performing segmentation in chest radiography, one would also need to contend with the different shape variations in organs due age, gender, disease and other health-related issues.

Mansoor et al. [1] presented a comprehensive survey discussing the challenges and accomplishments of the different segmentation methods for lungs which are reported in the literature. Several deep learning models based on fully convolutional networks have been investigated too. For instance, a network called InvertedNet is proposed to segment the heart, left and right clavicles, and lungs [4]. The well-established U-Net architecture has been utilized for segmenting the chest region and revealing promising results [8], [9], [49]. A model called structure correcting adversarial network (SCAN) was proposed as a generative adversarial network that uses convolutional layers for heart and lungs segmentation [10]. Moreover, traditional feature extraction methods are widely used for CXR imaging applications [1]. In [6], Ibragimov et al. proposed an approach for lung segmentation and landmark detection based on Haar-like features, a random forest classifier, and spatial relationships among landmarks.

B. Task 2: Bone and Rib Suppression

In chest X-ray images, the bone structure in the chest area is usually visible, which makes it hard for a radiologist to examine thoroughly the organs and assess any effects of a given disease accurately. Therefore, bone and rib suppression is exploited in order to suppress the appearance of bones in the chest X-ray images. One way to tackle the aforementioned problem is to utilize dual-energy subtraction (DES) imaging [27]. The DES imaging technique captures two or three radiography scans with two or three different energy-level of X-ray exposures. The captured images either highlight the soft tissues or bones based on the energy levels. Thus, the suppressed bone image will be estimated by combining the acquired images which include both the soft tissue-selective images and the bone-selective images [51]. Although effective in delineating the bone structure in the chest area, the DES imaging process has a number of shortcomings, among them is its more invasive nature due to the higher radiation dose and the presence of artifacts introduced in the acquisition process due to the effect of heartbeats.

Because of these aforementioned reasons, suppressing the bones in CXR images via traditional image processing techniques is considered safer and is shown to be more effective at overcoming the main challenges faced in CXR images. Along this line of research, a cascaded convolutional neural networks architecture (called CamsNet) [19] is proposed to predict the bone gradients in CXR images progressively with the ability of suppressing the bones as a consequence of these determined gradients. Another recent method is developed

by Chen *et al.* [12] which anatomically compensate the ribs and clavicles by specific multiple massive-training artificial neural networks (MTANNs) combined with total variation (TV) minimization smoothing along with a post-processing by histogram-matching. In another study, Gusarev et al. proposed two deep learning architectures to perform bone suppression and creating a soft tissue image. Considering bones as a noise level that is affecting these chest images [20], they tried to minimize the presence of this noise (i.e., bone) while still preserving the sharpness of the image for the eventual organ segmentation. In [57], many of the noise suppressing methods reviewed where the main objective in all these methods is to remove as much of the noise as possible while preserving most of the relevant details in the image. Another bone suppression method, based on deep adversarial networks and 2D Haar wavelet decomposition, has been proposed in [18]. Their method was mostly based on the theory of pix2pix network [38], a well-known conditional generative adversarial network. The pix2pix network is also used as the cornerstone of our proposed multitask model, which will be described in the section II. Bone suppression is also used as a pre-processing step, where bone suppressed CXR images are then feed the algorithms such as CheXNet in order to enhance the segmentation process and improve as a consequence the results of machine (automated) diagnosis [14]. The impact of bone suppression on machine diagnosis using deep learning networks have been thoroughly investigated and detailed in [21] and [16].

C. Joint Tasks via Multitask Learning

In multitask learning, multiple tasks are solved at the same time, while exploiting commonalities and differences across tasks. In comparison to training separate single task models, the multitask scheme can bring the following improvements [52].

- Improvement in results: Most often, coupling tasks makes the overall system achieve better results with respect to the desired accuracy. For example, in [53], a multitask learning approach based on deep convolutional networks is proposed for facial landmark detection with the auxiliary tasks of head pose estimation, gender classification and facial visibility, yielding more accurate results for each of the tasks.
- Improvement in learning efficiency: Efficiency of learning could include some aspects such as the number of required parameters, memory or storage requirements, computational time and training convergence rate. Obviously, fewer but optimal parameters and lower memory requirements are desirable in deploying such algorithms on conventional devices such as mobile phones and PCs [59].

In this research endeavor, we demonstrate that our method segments the organs while simultaneously suppressing the bone structure in CXR images. The proposed network is based on the well-known *pix2pix* network with promising results in the domain of image-to-image translation and segmentation

[38]. In order to incorporate the multitask objective, we propose to have an image-to-images translation machine. For this reason the pix2pix network and its implementation is modified to fit the need for multitasking (*pix2pix MT*). As far as the authors know, the proposed method as modified constitutes a first attempt at expanding the application of image-to-image network to image-to-images with the ability to generate more than one desired output. Furthermore, the dilated convolution technique [23] is employed in specific layers of the generator, which is shown to improve the results. All of the code and variations of this proposed model are shared online by the authors for other researchers to validate the merits of the proposed model on their own data or to replicate the results presented in this study. We refer to our model as *pix2pix MTdG* with the implication of multitask pix2pix with dilation in the generator.

More specifically, by feeding a CXR image to the pix2pix MTdG network, our model will generate automatically two output images simultaneously, which are the image of the bone suppressed lungs and the image containing the segmentation masks of the heart and lungs. Experimental results shows that the MTdG network yields promising and comparable results to the state-of-the-art methods that deal with these tasks individually. Results are evaluated with several metrics, including Dice and Jaccard scores, false negative and positive rates, peak signal-to-noise-ratio (PSNR) and structural similarity index (SSIM). The experimental results verified by 5-fold cross-validation and significance test exhibit promising outputs for both tasks.

The rest of this paper is organized as follows: Section II explains the proposed method and specifies the material used in conducting this study. The experimental results are presented and discussed in section III. Finally, the conclusion section IV provides a retrospective on what was accomplished through this novel approach.

II. MATERIALS & METHODS

A. Methodology

1) *Background*: In recent years, generative adversarial networks (GANs) and conditional generative adversarial networks (cGANs) have gained a lot of attention because of their superior performance in generation, segmentation, and translation empowered by adversarial scheme [35]. The GAN architecture consists of two adversarial models trained to work against each other: the generator aiming at generating an output and deceiving the discriminator and a discriminator component aiming at segregating the real output from the fake ones. In conditional mode (cGAN), both generator and discriminator are conditioned on ground truth labels or images. For example, in this study, the segmented organs and the bone suppressed images are the conditions and the generator is set up to generate this type of images.

The GANs are used extensively for segmentation in different applications with promising results [35], [38], [45]. An approach for segmenting and converting the clothes in images is proposed in [39] and a compact end-to-end cGAN network is proposed for real-time pixel-level segmentation of insulators in

high-voltage lines [42]. Detection and segmentation of roads, rivers, and areas for remote sensing are addressed via cGAN models in [40], [43], [46], [47]. Body parts are segmented by GAN to improve person identification [41] while cell membrane and nucleus are segmented by a cGAN in [44].

Generators of GANs are intended to learn the mapping from a random noise vector z to an output image y , *i.e.*, $G : z \Rightarrow y$ while cGANs are conditioned by an observed image x *i.e.*, $G : \{x, z\} \Rightarrow y$. The generator G would learn to produce outputs, which could not be distinguished as fake images by an adversarially trained discriminator, D . The objective of a GAN and that of a conditional GAN can be expressed through equations (1) and (2) respectively, where \mathbb{E} is the *Expectation* in the study population. Generator G tries to minimize this objective function against an adversarial D that tries to maximize it, *i.e.*, a *minimax* game as $\hat{G} = \arg \min_G \max_D \mathcal{L}_{GAN}$ and similarly $\hat{G} = \arg \min_G \max_D \mathcal{L}_{cGAN}$.

$$\begin{aligned} \mathcal{L}_{GAN}(G, D) = \\ \mathbb{E} [\log D(x, y)] + \mathbb{E} [\log(1 - D(G(x, z)))] \end{aligned} \quad (1)$$

$$\begin{aligned} \mathcal{L}_{cGAN}(G, D) = \\ \mathbb{E} [\log D(x, y)] + \mathbb{E} [\log(1 - D(x, G(x, z)))] \end{aligned} \quad (2)$$

2) *Proposed Model*: In this work, we have selected a conditional generative adversarial network, called pix2pix, an image-to-image translation network to use and modify for dealing our purposes [38]. The pix2pix is used in our method because:

- It shows promising prospects for accurate organ segmentation [38], [40], [44], [47].
- It is intrinsically a collection of filters and would be reasonable to perform bone and rib suppression as an image-to-image translation task [18].

The generator of pix2pix contains an auto-encoding network of convolutional layers with skip connections. The discriminator is also a convolutional network called PatchGAN discriminator, which attempts to determine whether each patch in an image is real or fake. The discriminator looks at the input/target pair and the input/output pair and produces its estimation on how realistic they look [38].

Figure 1 shows our model aiming to convert the input CXR image (In) into the desired output (T), which is the concatenation of desired targets, $Tt1$ as the organs' segmentation masks and $Tt2$ as the bone suppressed CXR image, *i.e.*, $T : Tt1 \parallel Tt2$ where \parallel shows concatenation in channel axis.

The input and output tensors of the generator network are In and $O : Ot1 \parallel Ot2$ where $Ot2$ is the output image corresponding to the bone suppression task and $Ot1$ is the image corresponding to the organ segmentation task which include the masks for the heart (colored red), left lung (colored blue), right lung (colored green) and background (colored black). In fact, the generator creates a tensor with 6 channels, which are the concatenation of $Ot1$ and $Ot2$.

The discriminator network acts in a similar fashion to PatchGAN in order to produce two output matrices, Odr and Odf corresponding to the real and fake input tensors. The fake tensor is a concatenation of CXR input image and outputs

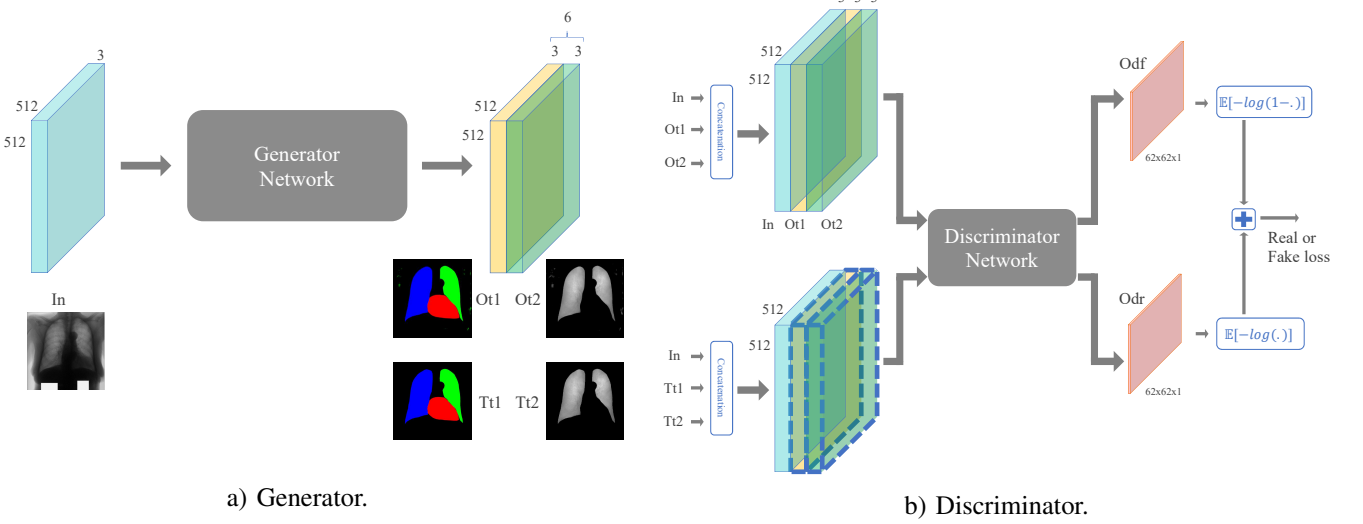


Fig. 1: Architecture of the presented image to images translation, multi-task pix2pix. In this figure, In , $Ot1$, $Ot2$, $Tt1$, $Tt2$ are the images of input CXR, targets of task 1 and task 2, output for task 1 and task 2, respectively. Notice that, all the images, input, output and target have three channels.

($In \parallel Ot1 \parallel Ot2$), and the real tensor is the concatenation of the CXR input image and targets ($In \parallel Tt1 \parallel Tt2$). If the discriminator is trained perfectly, it will create Odr matrix of 1 values and Odf matrix of 0 values. On the other side, if the generator is successful in fooling the discriminator, Odf would be a matrix of 1 values. Therefore, the loss functions for training the generator and discriminator are as equations (3) and (4) where $\|\cdot\|_1$ shows the $L1$ distance or norm.

$$\mathcal{L}_G = \mathbb{E}[-\log(Odf + \epsilon)] + \lambda \mathbb{E}[\|T - O\|_1] \quad (3)$$

$$\mathcal{L}_D = \mathbb{E}[-(\log(Odr + \epsilon) + \log(1 - Odf + \epsilon))] \quad (4)$$

Furthermore, to produce more efficient receptive fields, dilated convolutions [23] are utilized in some specific layers of the generator. The encoder of the generator consists of 8 layers and we use dilated convolutions with rate 2 in layers 2 to 7 in the proposed structure of the MTdG network. The effect of using and not using the dilated convolutional layers are contrasted in the results section.

B. Data

The Japanese Society of Radiological Technology (JSRT) is the only publicly available dataset which both desired tasks are available for it and is suitable for training and evaluating the proposed model. This dataset consists of CXR images collected by (JSRT) [22] and is publicly available in [24]. Segmentation masks for lungs and the heart were created later by [25] and are now available in [26]. The JSRT dataset comprises 247 CXRs, including images with and without lung nodules. All images have resolution of 2048×2048 in gray-scale with the color depth of 12 bits.

While there is no publicly available dataset for bone and rib suppression based on DES, Juhesz et al. developed a method for bone suppression [11]. Their results on the JSRT dataset have since became publicly available in [13]. We use this dataset to accomplish the second task of bone suppression.

As noted in CheXNet and through other investigations, the 512×512 resolution is sufficient for classifying lung-related diseases and nodule(s) localization [30], [32], [33], [36]. Therefore, we re-scaled the images of the dataset to 512×512 pixels because both tasks that are being accomplished have the potential to be used as new pre-processing methods for improving computer-aided diagnosis. The image intensities are also normalized by setting the minimum and maximum values to 0 and 255. In order to train the machine learning and especially the deep learning networks, it is essential to have enough number of samples that cover different variations [28], [29]. Therefore, the original images along with their corresponding masks and suppressed bone images were augmented by rotating them via 10 and -5 degrees, along with translations of (30, 10) and (-20, -10) pixels in reference to the (x,y) coordinates. Through this process, the size of the dataset has been increased by 5 times, to the total number of 1,235 images along with their corresponding ground-truths for the two tasks.

C. Implementation & Evaluation

The proposed model has been implemented based on the publicly available pix2pix code [37]. However, the code is modified to comply with the multi-tasking scenario.

For validation purposes, both the extended code that supports all these different variations¹ and the video showing this process at work are made available through the Internet to the research community². The method is evaluated using 5-fold cross-validation procedure in 4 different schemes as follows:

- Single task pix2pix network (p2p)
- Well-known u-net network (u-net)
- Multitask pix2pix network (p2p MT)

¹<https://github.com/mohaEs/image-to-images-translation>

²https://youtu.be/J8Uth26_7rQ

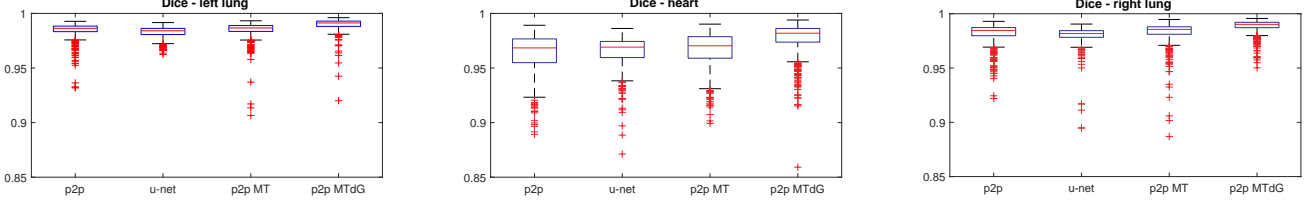


Fig. 2: Segmentation evaluation regarding to boxplots of Dice scores of tested methods.
(Left) left lung, (Middle) heart, (Right) right lung

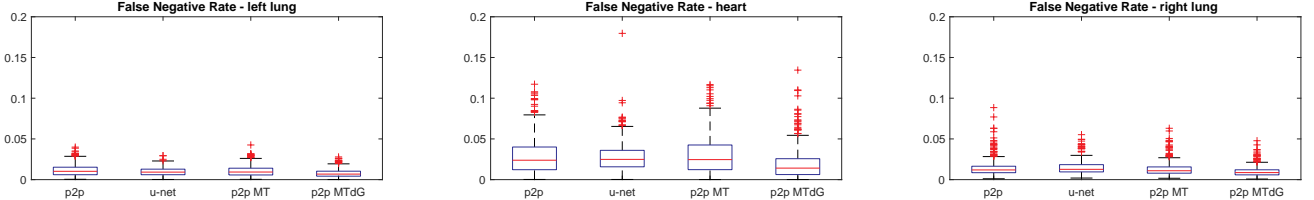


Fig. 3: Segmentation evaluation regarding to boxplots of false negative rates of tested methods.
(Left) left lung, (Middle) heart, (Right) right lung.

- Multitask pix2pix network with dilation in generator (p2p MTdG)

The network has been implemented using python and the tensorflow library. All computations for training the network have been performed on a system equipped by NVIDIA GPU Quadro M6000 with 24 GB memory. The MTdG network has 57,199,303 parameters to be trained and it takes almost 781 minutes for 335 epochs with a batch size of 20 samples. λ in equation 3 is set to 10 and learning rate of the Adam optimizer is set to 0.0002. The intensity channel of the input CXR image is replicated to support the CNN 3-channel RGB input data expectations. The size of the input/output images and kernel (or filter) are $512 \times 512 \times 3$ and 4×4 . To make a fair comparison with the results of the current state-of-art techniques, the resolution of 256×256 has been considered in this study as well.

III. RESULTS AND DISCUSSION

A. Task 1: Organ Segmentation

The segmented regions of the heart, the left lung and right lung generated by the model as output masks, are associated with the same regions in the ground-truth by using standard evaluation metrics in image processing, namely the Dice and Jaccard scores, false negative rate (FNR) and false positive rate (FPR). The Jaccard index is a metric that measures the percent overlap between the target mask (GT) and our prediction mask (PM). Jaccard metric is closely related to the Dice coefficient, which is not as easily described geometrically. False positive rate indicates the area ratio of predicted mask which had no associated ground truth mask and similarly false negative indicates the area ratio of ground truth mask which had no associated predicted mask. These standard evaluations metrics can be expressed mathematically as follow:

$$Jaccard = (PM \cap GT) / (PM \cup GT) \quad (5)$$

$$FNR = (!PM \cap GT) / GT \quad (6)$$

$$FPR = (PM \cap !GT) / GT \quad (7)$$

$$Dice = 2 \times (PM \cap GT) / (PM + GT) \quad (8)$$

Figures 2 and 3 show the box plots of the segmentation scores evaluated using the Dice and false negative rate of the heart, left and right lung for the different methods. It is worth noting that, the pix2pix MTdG has comparable and on average slightly superior results in comparison with the u-net network. However, the analysis carried out in this study, demonstrated that without dilation (p2p MT), the multi-task pix2pix might not be able to outperform the u-net network. The segmentation result of the proposed method (p2p MTdG) for the best and worst achieved Dice scores are shown in figure 4.

The average and standard deviation of the segmentation results, by all metrics, are summarized in Table I. Similarly, heart, left lung, right lung are considered separately with the overall average reported. The best achieved result is highlighted in blue, confirming that the multitask pix2pix with an embedded dilation in the generator (MTdG) surpasses all the other methods.

To the best of our knowledge, no multitask network has been found in the literature to benchmark the proposed multitask network for our tasks. A comparison between u-net (implemented by us) and MTdG along with the p-values of student's t-test is provided in Table I which clearly shows

³ All the details:

Up) Dice heart: 0.99, Jaccard heart: 0.99, FPR heart: 0.01, FNR heart: 0.01, dice right lung: 1.00, Jaccard right lung: 0.99, FPR right lung: 0.00 FNR right lung: 0.01, Dice left lung: 0.99, Jaccard left lung: 0.99, FPR left lung: 0.01, FNR left lung: 0.00.
Down) Dice heart: 0.86, Jaccard heart: 0.75, FPR heart: 0.31, FNR heart: 0.01, Dice right lung: 0.98, Jaccard right lung: 0.97, FPR right lung: 0.02, FNR right lung: 0.01, Dice left lung: 0.99, Jaccard left lung: 0.97, FPR left lung: 0.03, FNR left lung: 0.00.

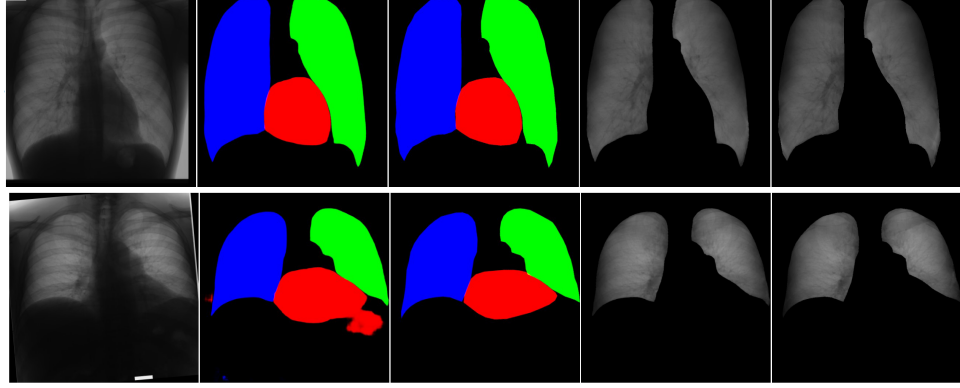


Fig. 4: Showing the results by proposed method according to the best and worst Dice scores. Columns left to right are, input image, segmentation result, segmentation target, bone suppression result, and bone suppression target.

Up) Best Dice: average of Dice, Jaccard, FPR and FNR are 0.99, 0.99, 0.01 and 0.01.

Down) Worst Dice: average of Dice, Jaccard, FPR and FNR are 0.94, 0.90, 0.12 and 0.01³.

TABLE I: Segmentation results of different methods. The best scores are colored blue.

		pix2pix	u-net	pix2pix MT	pix2pix MTdG	u-net vs. MTdG
Dice	Left lung	0.984 + 0.008	0.983 + 0.005	0.985 + 0.008	0.990 + 0.006	p-value = 1.2 e-93
	Heart	0.964 + 0.017	0.965 + 0.014	0.966 + 0.016	0.977 + 0.015	p-value = 3.6 e-57
	Right lung	0.982 + 0.009	0.980 + 0.009	0.983 + 0.010	0.988 + 0.006	p-value = 5.5 e-99
	Average	0.977 + 0.008	0.976 + 0.007	0.978 + 0.008	0.985 + 0.007	-
Jaccard	Left lung	0.969 + 0.014	0.967 + 0.010	0.971 + 0.015	0.980 + 0.011	p-value = 7.7 e-97
	Heart	0.931 + 0.032	0.933 + 0.026	0.935 + 0.030	0.956 + 0.027	p-value = 3.8 e-59
	Right lung	0.965 + 0.017	0.961 + 0.017	0.966 + 0.019	0.977 + 0.012	p-value = 6.9 e-105
	Average	0.955 + 0.016	0.953 + 0.013	0.957 + 0.015	0.971 + 0.013	-
FNR	Left lung	0.011 + 0.007	0.010 + 0.005	0.010 + 0.006	0.008 + 0.005	p-value = 8.8 e-18
	Heart	0.029 + 0.022	0.028 + 0.017	0.030 + 0.022	0.018 + 0.017	p-value = 7.1 e-24
	Right lung	0.014 + 0.009	0.015 + 0.008	0.013 + 0.008	0.010 + 0.006	p-value = 3.0 e-45
	Average	0.018 + 0.008	0.017 + 0.006	0.018 + 0.008	0.012 + 0.007	-
FPR	Left lung	0.020 + 0.018	0.024 + 0.013	0.020 + 0.018	0.013 + 0.013	p-value = 3.0 e-73
	Heart	0.044 + 0.036	0.043 + 0.033	0.038 + 0.033	0.028 + 0.029	p-value = 2.3 e-22
	Right lung	0.023 + 0.018	0.026 + 0.017	0.022 + 0.021	0.013 + 0.012	p-value = 8.3 e-67
	Average	0.071 + 0.017	0.031 + 0.015	0.027 + 0.016	0.018 + 0.013	-

TABLE II: Comparison the segmentation results of different methods on JSRT dataset.

Method	Image Size	Augmentation	Evaluation scheme	Dice	Jaccard	Dice	Jaccard
				Lungs	Heart	Lungs	Heart
Human observer [5]	2048×2048	No	-	-	0.946	-	0.887
InvertedNet [4]	256×256	No	3-fold CV	0.974	0.950	0.937	0.882
u-net by [9]	256×256	No	5-fold CV	0.976	0.962	-	-
u-net by [8]	256×256	No	5-fold CV	-	0.959	-	0.899
u-net by us	512×512	Yes	5-fold CV *	0.981	0.964	0.965	0.933
MTdG (proposed)	512×512	Yes	5-fold CV *	0.989	0.978	0.977	0.956
u-net by [49]	512×512	Yes	train/test split (80%/20%)**	0.986	-	-	-
SegNet by [9]	256×256	No	5-fold CV	0.979	0.955	0.944	0.896
SCAN [10]	400×400	No	train/test split (209/38)	0.973	0.947	0.927	0.866
FCN by [9]	256×256	No	5-fold CV	0.974	0.950	0.942	0.892
MTdG (proposed)	256×256	No	5-fold CV	0.974	0.962	0.934	0.928
MTdG (proposed)	256×256	No	3-fold CV	0.962	0.953	0.921	0.916
ASM tuned [5]	256×256	No	2-fold CV	-	0.927	-	0.814
Hybrid voting [5]	256×256	No	2-fold CV	-	0.949	-	0.86
Seghers et. al [7]	256×256	No	train/test split (50/44)	-	0.951	-	-
Ibragimov et. al [6]	-	No	-	-	0.953	-	-

*: p-values from significance test are reported in Table I.

**: JSRT dataset is not used for this work.

that the MTdG method yields better results with a significant difference ($p < 0.001$). However, to contrast these results with other methods in the literature, due to the variations in utilizing different folding schemes and image sizes, a fair comparison of the results is not a straightforward process.

The results of different state-of-the-art algorithms on the

JSRT dataset are summarized in Table II. The settings reported from each method are also provided in Table II with ‘-’ to mean that the value is not reported. For a fair comparison, the proposed method has also been tested using 256×256 image size, 3-fold cross-validation and without any augmentation. As presented in the Table, while the scores are really close

to each other, the best-achieved results are the ones provided by pix2pix MTdG in 512×512 image resolution. In all these other settings, the MTdG performance is still reasonable and is comparable to the performance of other techniques.

B. Task 2: Bone Suppression

The second task of the MTdG network is bone suppression. The results of this task are evaluated via the structural similarity index (SSIM) metric for similarity estimation, and the root mean squared error (RMSE) metric to measure the difference between predicted and actual values [34]. The RMSE measure between two X and Y images is expressed by Equation (9), where N in the total number of pixels in a image and i is the pixel counter. SSIM is a reference base quality assessment metric, which compares the local patterns of pixel intensities between the reference and output images. The maximum value of 1 implies that the two images are structurally similar, while a zero value indicates that there were no structural similarity. Usually the SSIM index is calculated via windowing on the images with 8×8 window size and 1 pixel striding. At the end, the mean of the computed values (MSSIM) would be reported. The MSSIM measure between two images X and Y and the default SSIM measure between two windows X_i and Y_i are as defined by Equations (10) and (11) where μ_{X_i} , μ_{Y_i} , $\sigma_{Y_i}^2$, $\sigma_{X_i}^2$, and $\sigma_{X_i Y_i}$ show the average of X_i , the average of Y_i , the variance of X_i , the variance of Y_i and the covariance of X_i

TABLE III: Results of bone suppression task via different methods.

	pix2pix	pix2pix MT	pix2pix MTdG
MSSIM	0.969 ± 0.009	0.968 ± 0.007	0.976 ± 0.006
RMSE	5.296 ± 1.688	5.382 ± 1.470	4.297 ± 1.046

and Y_i , respectively. The default settings of $c_1 = (0.01 L)^2$ and $c_2 = (0.03 L)^2$ are considered with L being the dynamic range of the pixel-values (i.e. 255 in our experiment).

$$RMSE(X, Y) = \sqrt{\frac{1}{N} \sum_{i=1}^N (x_i - y_i)^2} \quad (9)$$

$$MSSIM = \frac{1}{N} \sum_{i=1}^N SSIM(X_i, Y_i) \quad (10)$$

$$SSIM(X_i, Y_i) = \frac{(2\mu_{X_i}\mu_{Y_i} + c_1)(2\sigma_{X_i Y_i} + c_2)}{(\mu_{X_i}^2 + \mu_{Y_i}^2 + c_1)(\sigma_{X_i}^2 + \sigma_{Y_i}^2 + c_2)} \quad (11)$$

The box plots of the achieved MSSIMs and RMSEs for the different envisioned scenarios are shown in Figure 5 and Table III, proving the good performance of the proposed pix2pix MTdG method. The best and worst results with regards to the RMSE measure are shown in Figure 6.

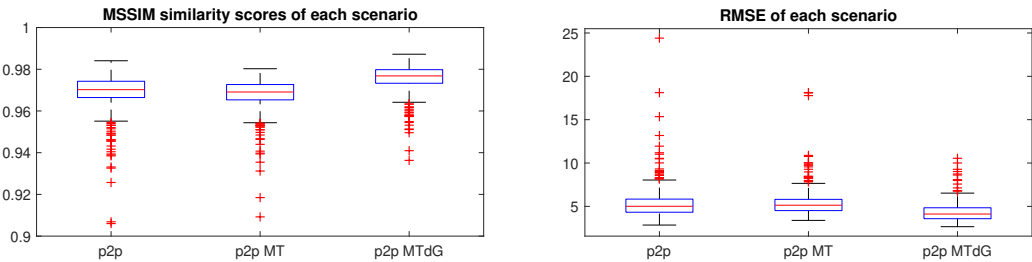


Fig. 5: Boxplots of the results of the bone suppression task. (Left) SSIM similarity score. (Right) RMSE difference.

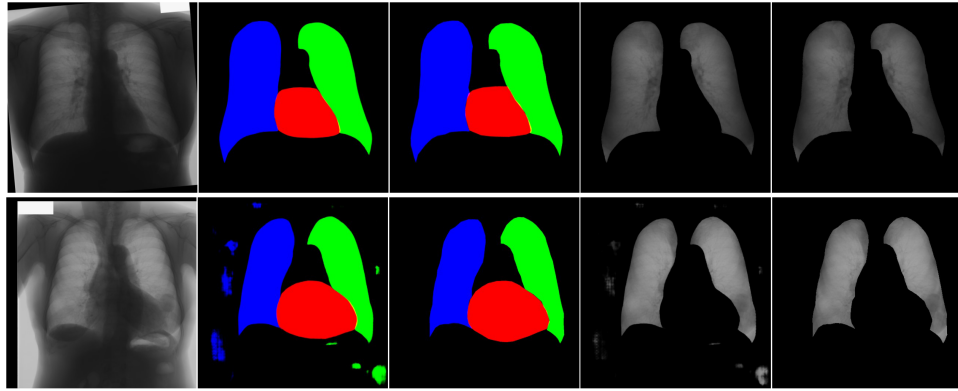


Fig. 6: Showing the bone suppression results by proposed method regarding to the best and worst RMSEs. Columns left to right: input image, segmentation result, segmentation target, bone suppression result and bone suppression target.

(Up) Best RMSE: SSIM: 0.99, RMSE : 2.66.

(Down) Worst RMSE: SSIM: 0.94, RMSE : 10.55.

TABLE IV: Summary of the properties of different methods.

		pix2pix	u-net	pix2pix MT	pix2pix MTdG
Task Segmentation	Average Dice	0.977 + 0.008	0.976 + 0.007	0.978 + 0.008	0.985 + 0.007
	Average FNR	0.018 + 0.008	0.017 + 0.006	0.018 + 0.008	0.012 + 0.007
Task Rib Suppression	Average MSSIM	0.969 + 0.009	-	0.968 + 0.007	0.976 + 0.006
	Average RMSE	5.296 + 1.688	-	5.382 + 1.470	4.297 + 1.046
	No. Parameters	$2 \times 57,190,084$	31,084,008	57,199,303	57,199,303
	Minimum Epochs	154	48	324	335
	Training time	$786 = 2 \times 393$ min	248 min	772	781

C. Discussion

As discussed earlier, the proposed pix2pix MTdG method provides promising results in accomplishing both segmentation and bone suppression tasks simultaneously. In this subsection, other characteristics of the proposed method are discussed and a summary of these results is provided in Table IV.

1) *Performance Analysis*: The performance of the proposed method is assessed here with respects to the results obtained and the network parameters that were considered. The following remarks can be made:

- As shown in Tables I and IV, the proposed multi-task pix2pix with dilation (MTdG) achieves the best results for both organ segmentation and bone suppression tasks.
- Using multitask pix2pix without dilation was not as effective for improving the results.
- Another advantage of MTdG is in the number of required parameters of the network, which is an intrinsic requirement for the multi-task pix2pix scheme. The trainable parameters of pix2pix, u-net, and multitask pix2pix are 57, 190, 084; 31, 084, 008 and 57, 199, 303, respectively. Note that the u-net architecture can only perform the seg-

mentation task. To employ two separate pix2pix networks for the two tasks, a large number of training parameters $2 \times 57, 190, 084$ would be needed. In other words, the performance of multitask pix2pix is reasonable in the number of parameters used while it maintains comparable good results to the state-of-the-art techniques.

- Nonetheless, the multitask pix2pix framework has one drawback, which is the number of required iteration/epochs for the training phase. In the experiments conducted in this study, MTdG required almost 300 epochs while u-net and single task pix2pix converged in only 50 and 150 epochs, meaning that the multitask framework requires more training time in comparison with other methods. It is worth noting that the above-mentioned facts are only true for the training process, that is, since a pre-trained network is used to generate the output, both methods perform similarly in the testing phase at the almost same time in only 1.2 seconds.

2) *Qualitative Analysis*: Figure 7 presents the segmentation results of the different methods for various subjects. From left to right, the image shown are the input image, the target image,

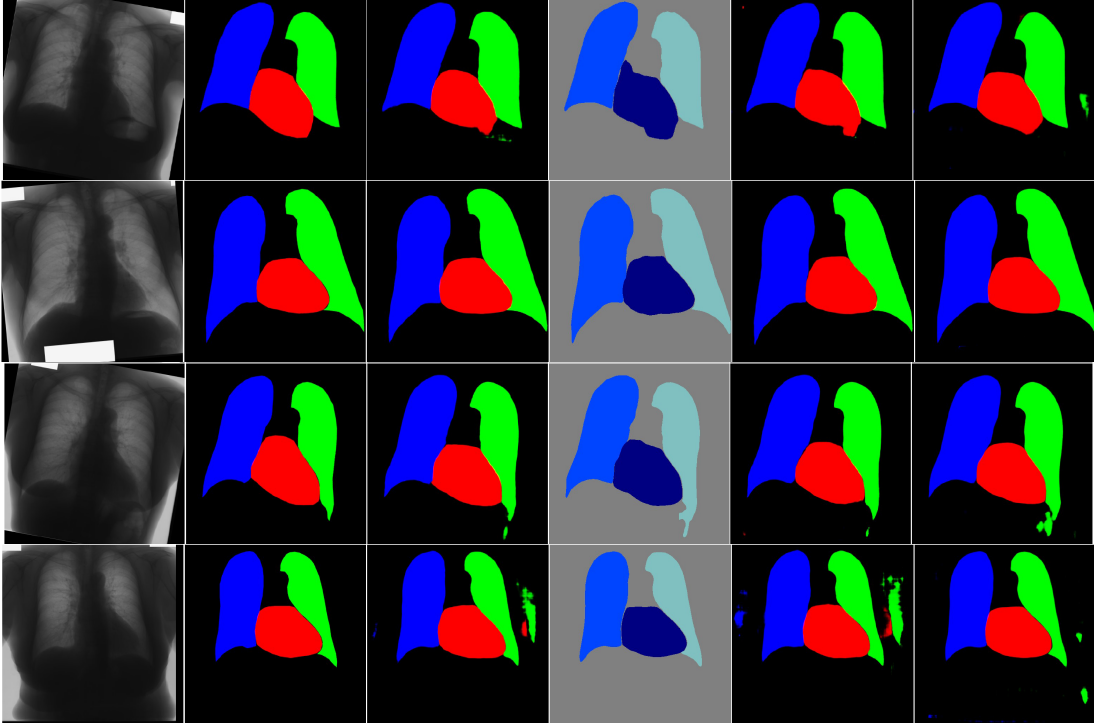


Fig. 7: Showing the segmentation results of different schemes for different subjects. Up to down are subjects and left to right are input, target, pix2pix, u-net, pix2pix MT and pix2pix MTdG.

pixp2ix output, u-net output, pix2pix MT output, and pix2pix MTdG output.

- As presented in the first row, the MTdG framework delivered the best outcomes in comparison with the other methods.
- However, the result of all the other methods in the second row is almost the same.
- The third row shows that the multitask pix2pix without dilation achieved better results in contrast to the other methods. This could be related to the fact that this dilation process may not be as effective in some specific cases. We intend to combine the layers with and without dilation as future work to see if the accuracy could be improved further.
- Moreover, as it is illustrated in the fourth row of Figure 7, the pix2pix based methods suffers from false positive segments such as isolated islands. Although this is the case for the u-net method as well, u-net demonstrates better results in this case. This could be associated with the fact that the loss function of u-net is addressing the segmentation constraints while the loss function of pix2pix is constructed to perform the pixel-wise comparison. This drawback could simply be removed by employing post-processing techniques such as connected components and considering the island area, which is not the aim of this paper at this juncture, but could be exploited in future work. Another approach to deal with this drawback is to implement segmentation related loss functions such as dice score to pix2pix loss function. While this technique was discussed by some authors in the literature, our investigations did not prove its efficiency in delivering any improvement to our case.

IV. CONCLUSION

Of all the different medical imaging modalities, X-ray imaging remains the most widely used imaging modality as it is the most cost effective and one of the easiest to administer. Chest X-ray remains an essential imaging modality for the diagnosis and follow up treatment of many diseases affecting the lungs, heart and bone structure within the chest area. In this study, a new deep learning based image-to-images approach was proposed that simultaneously segments the organs within the chest area and suppresses the bones that hinder the visibility and scrutiny of organs and nodules. In order to perform the these two essential tasks, the well-established pix2pix network is extended to generate two output images simultaneously (an image with bones suppressed, and a second image showing the segmented organs), yielding the new an image-to-images automated end-to-end framework instead of the traditional image-to-image approach that deals with each task individually. The proposed method was trained via an end-to-end fashion and is evaluated by cross validation and significance testing with several metrics, which showed promising results for both tasks. In summary, the contributions of this work can be summarized as follow:

- This work is the first to try to extend the application of image-to-image network to image-to-images architecture.

- The network is improved through the inclusion of dilated convolutions in some specific layers, which are shown to improve the results significantly.
- The image-to-images network is used to accomplish simultaneously the two common and most needed tasks of bone suppression and organ segmentation in CXR image.
- All of the developed code is shared publicly online for validation purposes and for use by the research community interested in the automated diagnosis and in treatment follow up using chest X rays.

REFERENCES

- [1] Mansoor, A., Bagci, U., Foster, B., Xu, Z., Papadakis, G.Z., Folio, L.R., Udupa, J.K. and Mollura, D.J., 2015. Segmentation and image analysis of abnormal lungs at CT: current approaches, challenges, and future trends. *RadioGraphics*, 35(4), pp.1056-1076.
- [2] Qin, C., Yao, D., Shi, Y. and Song, Z., 2018. Computer-aided detection in chest radiography based on artificial intelligence: a survey. *Biomedical engineering online*, 17(1), p.113.
- [3] Santosh, K.C. and Antani, S., 2017. Automated chest x-ray screening: Can lung region symmetry help detect pulmonary abnormalities?. *IEEE transactions on medical imaging*, 37(5), pp.1168-1177.
- [4] Novikov, A.A., Lenis, D., Major, D., Hladvka, J., Wimmer, M. and Bhler, K., 2018. Fully convolutional architectures for multiclass segmentation in chest radiographs. *IEEE transactions on medical imaging*, 37(8), pp.1865-1876.
- [5] Van Ginneken, B., Stegmann, M.B. and Loog, M., 2006. Segmentation of anatomical structures in chest radiographs using supervised methods: a comparative study on a public database. *Medical image analysis*, 10(1), pp.19-40.
- [6] Ibragimov, B., Likar, B., Pernu, F. and Vrtovec, T., 2016, April. Accurate landmark-based segmentation by incorporating landmark misdetections. In 2016 IEEE 13th International Symposium on Biomedical Imaging (ISBI) (pp. 1072-1075). IEEE.
- [7] Seghers, D., Loeckx, D., Maes, F., Vandermeulen, D. and Suetens, P., 2007. Minimal shape and intensity cost path segmentation. *IEEE Transactions on Medical Imaging*, 26(8), pp.1115-1129.
- [8] Wang, C., 2017, June. Segmentation of multiple structures in chest radiographs using multi-task fully convolutional networks. In Scandinavian Conference on Image Analysis (pp. 282-289). Springer, Cham.
- [9] Oliveira, H. and dos Santos, J., 2018, October. Deep Transfer Learning for Segmentation of Anatomical Structures in Chest Radiographs. In 2018 31st SIBGRAPI Conference on Graphics, Patterns and Images (SIBGRAPI) (pp. 204-211). IEEE.
- [10] Dai, W., Dong, N., Wang, Z., Liang, X., Zhang, H. and Xing, E.P., 2018. SCAN: Structure correcting adversarial network for organ segmentation in chest X-rays. In Deep Learning in Medical Image Analysis and Multimodal Learning for Clinical Decision Support (pp. 263-273). Springer, Cham.
- [11] Juhsz, S., Horvth, ., Nikhzy, L. and Horvth, G., 2010. Segmentation of anatomical structures on chest radiographs. In XII Mediterranean Conference on Medical and Biological Engineering and Computing 2010 (pp. 359-362). Springer, Berlin, Heidelberg.
- [12] Chen, S. and Suzuki, K., 2013. Separation of bones from chest radiographs by means of anatomically specific multiple massive-training ANNs combined with total variation minimization smoothing. *IEEE transactions on medical imaging*, 33(2), pp.246-257.
- [13] Bone suppressed JSRT dataset, <https://www.mit.bme.hu/eng/events/2013/04/18/bone-shadow-eliminated-images-jsrt-database> , <https://www.kaggle.com/hmchuong/xray-bone-shadow-supression>, Accessed: 2019-01-30
- [14] Huynh, M.C., Nguyen, T.H. and Tran, M.T., 2018, November. Context Learning for Bone Shadow Exclusion in CheXNet Accuracy Improvement. In 2018 10th International Conference on Knowledge and Systems Engineering (KSE) (pp. 135-140). IEEE.
- [15] Orbn, G., Horvth, . and Horvth, G., 2010. Lung nodule detection on rib eliminated radiographs. In XII Mediterranean Conference on Medical and Biological Engineering and Computing 2010 (pp. 363-366). Springer, Berlin, Heidelberg.

[16] Gordienko, Y., Gang, P., Hui, J., Zeng, W., Kochura, Y., Alienin, O., Rokovyi, O. and Stirenko, S., 2018, January. Deep learning with lung segmentation and bone shadow exclusion techniques for chest x-ray analysis of lung cancer. In International Conference on Computer Science, Engineering and Education Applications (pp. 638-647). Springer, Cham.

[17] Gordienko, Y., Kochura, Y., Alienin, O., Rokovyi, O., Stirenko, S., Gang, P., Hui, J. and Zeng, W., 2018. Dimensionality reduction in deep learning for chest x-ray analysis of lung cancer. arXiv preprint arXiv:1801.06495.

[18] Oh, D.Y. and Yun, I.D., 2018. Learning Bone Suppression from Dual Energy Chest X-rays using Adversarial Networks. arXiv preprint arXiv:1811.02628.

[19] Yang, W., Chen, Y., Liu, Y., Zhong, L., Qin, G., Lu, Z., Feng, Q. and Chen, W., 2017. Cascade of multi-scale convolutional neural networks for bone suppression of chest radiographs in gradient domain. Medical image analysis, 35, pp.421-433.

[20] Gusarev, M., Kuleev, R., Khan, A., Rivera, A.R. and Khattak, A.M., 2017, August. Deep learning models for bone suppression in chest radiographs. In 2017 IEEE Conference on Computational Intelligence in Bioinformatics and Computational Biology (CIBCB) (pp. 1-7). IEEE.

[21] Baltruschat, I.M., Steinmeister, L., Ittrich, H., Adam, G., Nickisch, H., Saalbach, A., von Berg, J., Grass, M. and Knopp, T., 2018. When does Bone Suppression and Lung Field Segmentation Improve Chest X-Ray Disease Classification?. arXiv preprint arXiv:1810.07500.

[22] Shiraishi, J., Katsuragawa, S., Ikezoe, J., Matsumoto, T., Kobayashi, T., Komatsu, K.I., Matsui, M., Fujita, H., Kodera, Y. and Doi, K., 2000. Development of a digital image database for chest radiographs with and without a lung nodule: receiver operating characteristic analysis of radiologists' detection of pulmonary nodules. American Journal of Roentgenology, 174(1), pp.71-74.

[23] Wang, P., Chen, P., Yuan, Y., Liu, D., Huang, Z., Hou, X. and Cottrell, G., 2018, March. Understanding convolution for semantic segmentation. In 2018 IEEE Winter Conference on Applications of Computer Vision (WACV) (pp. 1451-1460). IEEE.

[24] JSRT dataset, <http://db.jsrt.or.jp/eng.php>, Accessed: 2019-01-30

[25] Van Ginneken, B., Stegmann, M.B. and Loog, M., 2006. Segmentation of anatomical structures in chest radiographs using supervised methods: a comparative study on a public database. Medical image analysis, 10(1), pp.19-40.

[26] JSRT segmentation dataset, <https://www.isi.uu.nl/Research/Databases/SCR/>, Accessed: 2019-01-30

[27] Vock, P. and Szucs-Farkas, Z., 2009. Dual energy subtraction: principles and clinical applications. European journal of radiology, 72(2), pp.231-237.

[28] Perez, L. and Wang, J., 2017. The effectiveness of data augmentation in image classification using deep learning. arXiv preprint arXiv:1712.04621.

[29] Shi, H., Wang, L., Ding, G., Yang, F. and Li, X., 2018, August. Data Augmentation with Improved Generative Adversarial Networks. In 2018 24th International Conference on Pattern Recognition (ICPR) (pp. 73-78). IEEE.

[30] Rajpurkar, P., Irvin, J., Ball, R.L., Zhu, K., Yang, B., Mehta, H., Duan, T., Ding, D., Bagul, A., Langlotz, C.P. and Patel, B.N., 2018. Deep learning for chest radiograph diagnosis: A retrospective comparison of the CheXNeXt algorithm to practicing radiologists. PLoS medicine, 15(11), p.e1002686.

[31] Rajpurkar, P., Irvin, J., Zhu, K., Yang, B., Mehta, H., Duan, T., Ding, D., Bagul, A., Langlotz, C., Shpanskaya, K. and Lungren, M.P., 2017. CheXnet: Radiologist-level pneumonia detection on chest x-rays with deep learning. arXiv preprint arXiv:1711.05225.

[32] Gozes, O. and Greenspan, H., 2018. Lung Structures Enhancement in Chest Radiographs via CT Based FCNN Training. In Image Analysis for Moving Organ, Breast, and Thoracic Images (pp. 147-158). Springer, Cham.

[33] Qu, K., Chai, X., Liu, T., Zhang, Y., Leng, B. and Xiong, Z., 2017, November. Computer-Aided Diagnosis in Chest Radiography with Deep Multi-Instance Learning. In International Conference on Neural Information Processing (pp. 723-731). Springer, Cham.

[34] Jagalingam, P. and Hegde, A.V., 2015. A review of quality metrics for fused image. Aquatic Procedia, 4, pp.133-142.

[35] Yi, X., Walia, E. and Babyn, P., 2018. Generative adversarial network in medical imaging: A review. arXiv preprint arXiv:1809.07294.

[36] Ding, M., Antani, S., Jaeger, S., Xue, Z., Candemir, S., Kohli, M. and Thoma, G., 2017, March. Local-global classifier fusion for screening chest radiographs. In Medical Imaging 2017: Imaging Informatics for Healthcare, Research, and Applications (Vol. 10138, p. 101380A). International Society of Optics and Photonics.

[37] Eslami, M., Neuschafer-Rube, C. and Serrurier, A., Automatic Vocal Tract Segmentation based on Conditional Generative Adversarial Neural Network.

[38] Isola, P., Zhu, J.Y., Zhou, T. and Efros, A.A., 2017. Image-to-image translation with conditional adversarial networks. In Proceedings of the IEEE conference on computer vision and pattern recognition (pp. 1125-1134).

[39] Zhang, H., Sun, Y., Liu, L., Wang, X., Li, L. and Liu, W., 2018. ClothIn- gOut: a category-supervised GAN model for clothing segmentation and retrieval. Neural Computing and Applications, pp.1-12.

[40] Wang, X., Yan, H., Huo, C., Yu, J. and Pant, C., 2018, August. Enhancing Pix2Pix for Remote Sensing Image Classification. In 2018 24th International Conference on Pattern Recognition (ICPR) (pp. 2332-2336). IEEE.

[41] Zhao, G., Jiang, J., Liu, J., Yu, Y. and Wen, J.R., 2018, July. Improving Person Re-identification by Body Parts Segmentation Generated by GAN. In 2018 International Joint Conference on Neural Networks (IJCNN) (pp. 1-8). IEEE.

[42] Chang, W., Yang, G., Yu, J. and Liang, Z., 2018. Real-time segmentation of various insulators using generative adversarial networks. IET Computer Vision, 12(5), pp.596-602.

[43] Lopez-Fuentes, L., Rossi, C. and Skinnemoen, H., 2017, December. River segmentation for flood monitoring. In 2017 IEEE International Conference on Big Data (Big Data) (pp. 3746-3749). IEEE.

[44] Sato, M., Hotta, K., Imanishi, A., Matsuda, M. and Terai, K., 2018. Segmentation of Cell Membrane and Nucleus by Improving Pix2pix. In BIOSIGNALS (pp. 216-220).

[45] Zhu, X., Zhang, X., Zhang, X.Y., Xue, Z. and Wang, L., 2019. A novel framework for semantic segmentation with generative adversarial network. Journal of Visual Communication and Image Representation, 58, pp.532-543.

[46] Han, X., Lu, J., Zhao, C., You, S. and Li, H., 2018. Semisupervised and weakly supervised road detection based on generative adversarial networks. IEEE Signal Processing Letters, 25(4), pp.551-555.

[47] Kniaz, V.V., 2018, October. Conditional GANs for semantic segmentation of multispectral satellite images. In Image and Signal Processing for Remote Sensing XXIV (Vol. 10789, p. 107890R). International Society for Optics and Photonics.

[48] Diamant, I., Bar, Y., Geva, O., Wolf, L., Zimmerman, G., Lieberman, S., Konen, E. and Greenspan, H., 2017. Chest radiograph pathology categorization via transfer learning. In Deep Learning for Medical Image Analysis (pp. 299-320). Academic Press.

[49] Islam, J. and Zhang, Y., 2018. Towards Robust Lung Segmentation in Chest Radiographs with Deep Learning. arXiv preprint arXiv:1811.12638.

[50] Wang, H. and Xia, Y., 2018. Chestnet: A deep neural network for classification of thoracic diseases on chest radiography. arXiv preprint arXiv:1807.03058.

[51] Martini, K., Baessler, M., Baumueller, S. and Frauenfelder, T., 2017. Diagnostic accuracy and added value of dual-energy subtraction radiography compared to standard conventional radiography using computed tomography as standard of reference. PloS one, 12(3), p.e0174285.

[52] Zhang, Y. and Yang, Q., 2017. A survey on multi-task learning. arXiv preprint arXiv:1707.08114.

[53] Ranjan, R., Patel, V.M. and Chellappa, R., 2017. Hyperface: A deep multi-task learning framework for face detection, landmark localization, pose estimation, and gender recognition. IEEE Transactions on Pattern Analysis and Machine Intelligence, 41(1), pp.121-135.

[54] Raoof, S., Feigin, D., Sung, A., Raoof, S., Irugulpati, L. and Rosenow III, E.C., 2012. Interpretation of plain chest roentgenogram. Chest, 141(2), pp.545-558.

[55] Ruuskanen, O., Lahti, E., Jennings, L.C. and Murdoch, D.R., 2011. Viral pneumonia. The Lancet, 377(9773), pp.1264-1275.

[56] Neal, R.D., Barham, A., Bongard, E., Edwards, R.T., Fitzgibbon, J., Griffiths, G., Hamilton, W., Hood, K., Nelson, A., Parker, D. and Porter, C., 2017. Immediate chest X-ray for patients at risk of lung cancer presenting in primary care: randomised controlled feasibility trial. British journal of cancer, 116(3), p.293.

[57] Mafi, M., Martin, H., Cabrerizo, M., Andrian, J., Barreto, A. and Adjouadi, M., 2018. A comprehensive survey on impulse and Gaussian denoising filters for digital images. Signal Processing.

[58] Goryawala, M., Gulec, S., Bhatt, R., McGoron, A.J. and Adjouadi, M., 2014. A low-interaction automatic 3D liver segmentation method using computed tomography for selective internal radiation therapy. BioMed research international, 2014.

[59] Sze, V., Chen, Y.H., Emer, J., Suleiman, A. and Zhang, Z., 2017, April. Hardware for machine learning: Challenges and opportunities. In 2017 IEEE Custom Integrated Circuits Conference (CICC) (pp. 1-8). IEEE.